Nano Research

Open Access

Research Article

Programmable artificial chaperone for aging intervention

Tiantian Wu[1,2] ✉, Shun Zhang[2], Le Li[2], Chen Li[1,2], Pengxuan Zhao[2], Xiaoyuan Chen[3] ✉, and Junjie Cheng[4] ✉

[1] *Hainan Academy of Medical Sciences, Hainan Medical University, 3 Xueyuan Road, Haikou 571199, China*
[2] *NHC Key Laboratory of Tropical Disease Control, School of Life Sciences and Medical Technology, College of Pharmacy, Hainan Medical University, Haikou 571199, China*
[3] *Center for Nuclear Medicine and Molecular Imaging (CNMMI), Shandong Cancer Hospital and Institute, Jinan 250117, China*
[4] *Department of Nutrition and Food Hygiene, School of Public Health, Southeast University, Nanjing 210009, China*

Cite this article: *Nano Research*, **2026**, *19*, 94908731. https://doi.org/10.26599/NR.2026.94908731

ABSTRACT: Aging is marked by a decline in cellular proteostasis, leading to protein misfolding, oxidative modifications, and aggregation, thereby impairing cellular function and accelerating senescence-related deterioration. Strengthening proteostasis networks can mitigate these disruptions and restore cellular homeostasis. Here, a programmable DNA building blocks-based artificial chaperone, Th^{Ribo}, was constructed to selectively target ribosomes and employ a reductive repair cascade that prevents misfolding and aggregation caused by oxidative post-translational modifications (oxidative PTMs) of newly synthesized proteins, repairs already damaged residues, and restores proteostasis balance. In aging mice, Th^{Ribo} effectively suppressed senescence-associated signaling pathways, including the canonical tumor protein p53 (p53)/p21/p16 axis and the stress-responsive c-Jun N-terminal kinase (JNK) pathway, improved brain protein homeostasis, reduced oxidative stress markers, enhanced motor performance, and exhibited desirable biocompatibility. This ribosome-targeted, programmable artificial chaperone provides a versatile platform for maintaining proteostasis and is expected to offer a promising strategy for anti-aging interventions.

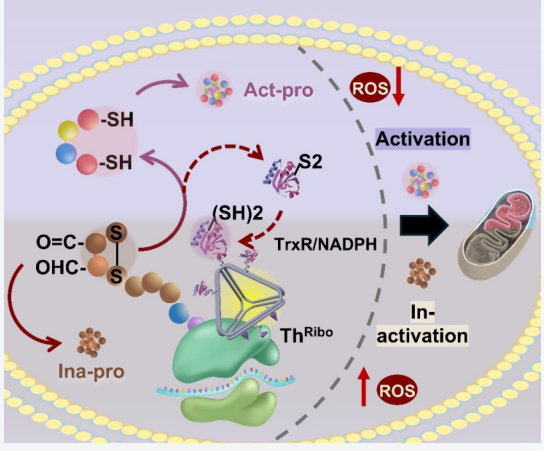

KEYWORDS: nanomedicine, DNA nanotechnology, DNA biomaterials, nucleic acids chemistry, drug and gene delivery

1 Introduction

Aging is characterized by a progressive decline in cellular proteostasis, marked by protein misfolding, oxidative modifications, and aggregation, which are closely associated with various senescence-related protein misfolding diseases [1, 2]. Moreover, excessive accumulation of reactive oxygen species (ROS) in aging cells can directly damage peptide moieties, including amino acid side chains, peptide bonds, and the polypeptide backbone [3]. Oxidative modifications of amino acid side chains, such as carbonylation, thiol oxidation, and disulfide disruption, cause profound structural alterations, including disruption of native folds, formation of inter- or intra-molecular crosslinks, and protein aggregation [4–6]. These changes ultimately impair protein function and exacerbate cellular degeneration [3, 7–10].

Ribosomes are the central machinery for protein synthesis, and their efficiency, translation kinetics, and co-translational folding regulation directly determine the stability and function of nascent polypeptides [1, 11]. Consequently, the ribosome serves as a primary hub for protein quality control, where ribosome-associated quality control mechanisms actively monitor and resolve translation errors to prevent the accumulation of aberrant polypeptides [7, 12]. Targeting the ribosome thus represents a proactive strategy to rectify proteostatic failures at the source, rather than merely managing downstream aggregates [13]. After emerging from the ribosome, nascent polypeptide chains must fold into their correct three-dimensional structures within a complex cellular environment, a process essential for their biological activity and cellular function [14, 15]. Molecular chaperones, though not defining the final folded state, are crucial for protein biogenesis and proteostasis [16, 17]. They associate with nascent chains or early folding intermediates to block non-productive interactions and

Received: January 6, 2026; **Revised:** April 8, 2026
Accepted: April 10, 2026

✉Address correspondence to Tiantian Wu, sa19071@mail.ustc.edu.cn; Xiaoyuan Chen, chen9647@gmail.com; Junjie Cheng, jjcheng@seu.edu.cn, jjcheng@ustc.edu.cn

aggregation, guiding correct folding pathways and promoting the efficient generation of functional proteins [15, 18, 19]. Thus, rationally reinforcing or mimicking molecular chaperone activity are practical strategies to sustain proteostasis in aging cells.

DNA nanotechnology exploits the predictable and programmable Watson–Crick base pairing of DNA to construct nanostructures with well-defined dimensions, shapes, and topologies [20]. These nanostructures exhibit unique biocompatibility and programmability, but more critically, allow site-specific anchoring and assembly of active building blocks, such as aptamers, siRNAs, deoxyribozymes (DNAzymes), or non-nucleic acid ligands like polymers and peptides, to form integrated, plug-and-play targeting systems [21–27]. However, achieving precise ribosome intervention remains a formidable challenge for existing delivery systems. Conventional strategies often suffer from off-target effects and a lack of spatial precision, which can disrupt global translation and induce cytotoxicity [28]. Furthermore, the dense ribosomal architecture and complex cellular environment impose significant steric and electrostatic barriers to efficient targeting [29, 30]. Pioneering studies have demonstrated DNA nanostructures capable of targeting ribosomes and enhancing intracellular modulation efficiency [31], providing a precedent for using DNA nanostructures to target ribosomes. The programmability and spatial precision of these platforms allow the design of ribosome-targeted artificial chaperones that modulate proteostasis at the organelle scale, directly from the source of protein synthesis.

In this study, a programmable DNA tetrahedron-based artificial chaperone (Th^{Ribo}, Scheme 1) was constructed through self-assembling DNA strands with orientationally anchored His-thioredoxin (HTrx) for ribosome-targeted intervention. The addressable DNA tetrahedron developed by our group served as the carrier, with an optimized specific binding probe at its base [32, 33]. Recombinant HTrx grafted onto the tetrahedron vertices effectively shields nascent polypeptides from oxidative damage and assists proper folding under ribosome guidance. Following cellular internalization and ribosome recognition, Th^{Ribo} initiates a reductive repair cascade to protect newly synthesized proteins, repair oxidized residues, and maintain proteostasis. In aging mouse models, Th^{Ribo} administration effectively improved protein homeostasis, alleviated aging-related indicators, and rescued functional deficits. To our knowledge, this is the first artificial chaperone constructed via DNA nanotechnology that integrates a ribosome-targeting probe, which is expected to provide a promising strategy for the development of anti-aging nanomedicine interventions.

2 Results and discussion

2.1 Construction and characterization of the artificial chaperone Th^{Ribo}

The artificial chaperone, namely Th^{Ribo}, was synthesized by hybridizing single-strand DNA-modified HTrx (HTrx-S) with pre-assembled DNA vertex (V-1, V-2, V-3, and V-4 as shown in Scheme 1 and Figs. S1–S4 in the Electronic Supplementary Material (ESM)). We at first constructed the recombinant HTrx with an N-terminal His_6-tag for purification and a C-terminal-$(GS)_3$-C for conjugation using molecular cloning technology (Fig. S5 in the ESM). As described in our previous research [34], HTrx with extra-SH on the cysteine at the C-terminal was coupled to 5' NH_2-labeled

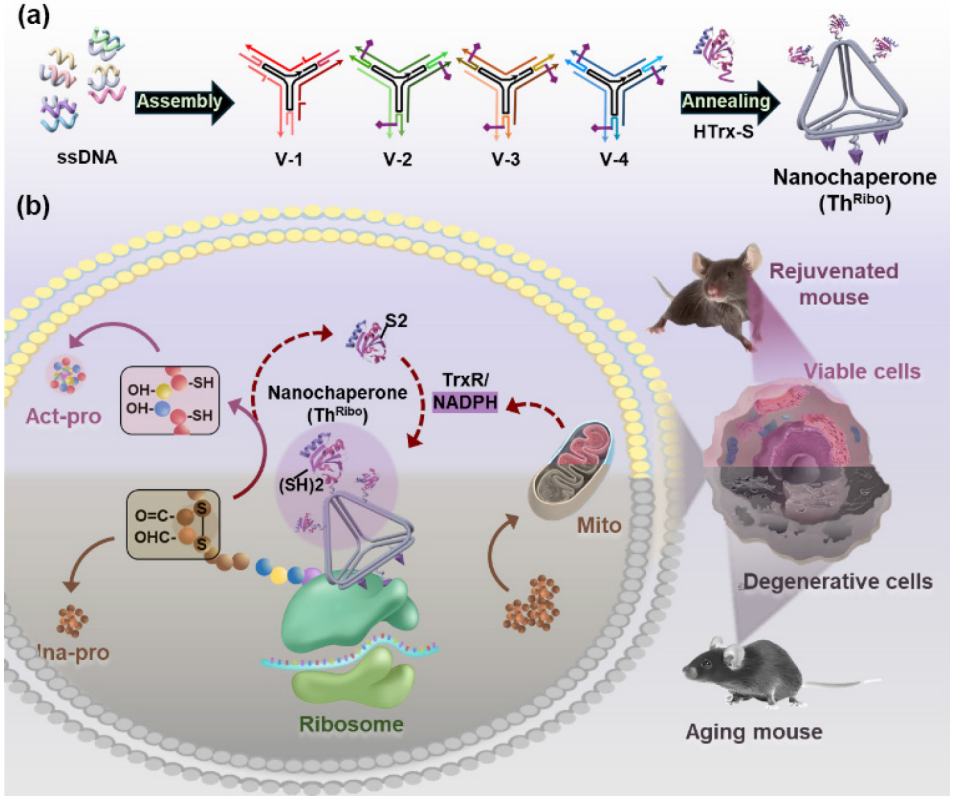

Scheme 1 Schematic illustration of the DNA nanochaperone Th^{Ribo} for ribosome-targeted proteostasis maintaining. (a) Construction of the addressable double-bundle DNA tetrahedron-based nanostructure. The recombinant HTrx was conjugated with ssDNA and precisely hybridized to the DNA tetrahedron with specific number. (b) The proposed mechanism of Th^{Ribo} for proteostasis maintaining under oxidative stress in aging cells.

ssDNA strand using classic sulfo-SMCC conjugation strategy, and the HTrx-S was obtained through purification using gel filtration through an ÄKTA purifier system (ÄKTA) (Fig. S6 in the ESM). Then, the two-step assembly as illustrated was conducted to synthesize the Th^{Ribo}. The addressable double-bundle DNA tetrahedron as the nanocarrier for the construction of the nanochaperone was based on the original design of our group. We rationally modified the DNA tetrahedron using three copies of capture for hybridizing the HTrx-S at the V-1 as shown in the ESM to be dispersedly grafted onto the vertices of a tetrahedral structure, and using different copies of ribosome-targeted probe to test the ribosome-specific binding (Figs. 1(a) and 1(b), and Fig. S7 in the ESM). ThR1 (one copy), ThR3 (three copies), and ThR6 (six copies) were labeled with black hole quencher (BHQ) probe and added to Cy5-modified shortened 28S rRNA (s28S) with the same ribosome-targeted probe concentration. As shown in the results of fluorescence spectra, ThR6 exhibited the best fluorescence quenching effect under the indicated experimental conditions, which indicates ThR6 holds the greatest potential in ribosome binding; therefore, we chose six copies of ribosome-targeted probe to construct the nanochaperone (Figs. 1(c) and 1(d)). The delayed migration of the electrophoretic band and perfect merge of fluorescein isothiocyanate (FITC)-labeled HTrx (green) signal and Cy5-labeled DNA tetrahedron signal demonstrated that the rationally designed Th^{Ribo} was successfully constructed (Fig. 1(e)). The clear triangle-like morphology was imaged by atomic force microscopy (AFM) (Fig. 1(f)). No aggregation or disassembly occurred in the preparation of the Th^{Ribo}. Furthermore, efficient binding of Th^{Ribo} with s28S and extracted ribosome was confirmed by agarose gel electrophoresis (Fig. 1(g), and Figs. S8 and S9 in the ESM), and negligible effect on the binding curve was detected according to the fluorescence spectra (Fig. 1(h)). Consistent with the AFM analysis, the diameter measured by dynamic light scattering (DLS) showed that the HTrx-conjugated Th^{Ribo} (20.3 ± 3.3 nm) was slightly larger than ThR6 (18.9 ± 4.1 nm) owing to the successful HTrx-S hybridization (Fig. 1(i)). The stability of Th^{Ribo} under physiological conditions was verified in Dulbecco's modified Eagle medium (DMEM) containing 200 μM H_2O_2 or serum, and no aggregation or degradation was detected during the 24 h of incubation (Fig. 1(j) and Fig. S10 in the ESM). Additionally, effective cell internalization was imaged by confocal laser scanning microscopy (CLSM) (Fig. 1(k)). To quantitatively evaluate the intracellular ribosome-targeting capability, we performed co-localization analysis using an anti-ribosomal protein lateral stalk subunit P0 (RPLPO) antibody (Fig. S11 in the ESM). Confocal microscopy revealed a high Pearson's correlation coefficient of

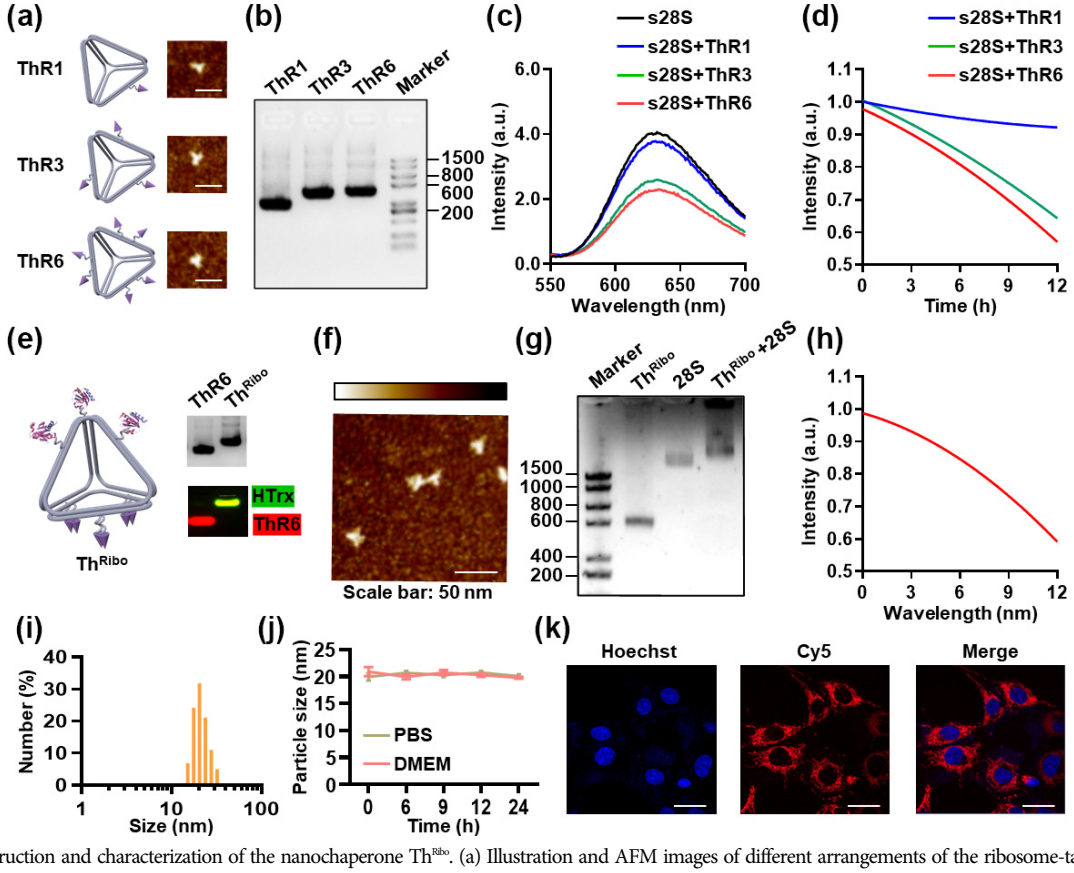

Figure 1 Construction and characterization of the nanochaperone Th^{Ribo}. (a) Illustration and AFM images of different arrangements of the ribosome-targeted probe on the bottom of the DNA tetrahedron. Different numbers of ribosome-targeted probes (ThR1: one copy; ThR3: three copies; ThR6: six copies) were conjugated through hybridization. Scale bars: 50 nm. (b) 1.5% agarose gel electrophoresis of ThR1, ThR3, and ThR6. Samples were separated in 1× TAE/Mg^{2+} buffer (pH = 8.3). (c) Fluorescence spectra of the mixture of Cy5-modified shortened 28S rRNA (s28S) and DNA tetrahedron with BHQ-labeled ribosome-targeted probe. The mixture containing the same concentration of the ribosome-targeted probes was cultured at 37 °C for 12 h. (d) Kinetics analysis of the binding of DNA tetrahedron with s28S. (e) 1.5% agarose gel electrophoresis of ThR6 and HTrx-loaded Th^{Ribo}. In fluorescence imaging, HTrx was labeled with FITC (green) and the DNA tetrahedron was labeled with Cy5 (red). (f) AFM images of Th^{Ribo}. Scale bar: 50 nm. (g) 1.0% agarose gel electrophoresis of Th^{Ribo}, S28 rRNA, and the mixture of Th^{Ribo} and S28 rRNA. (h) Kinetics analysis of the binding of Cy5-modified sS28 and Th^{Ribo} with BHQ-labeled ribosome-targeted probe. (i) Hydrodynamic diameters of Th^{Ribo} measured by DLS. (j) Stability analysis of Th^{Ribo} in DMEM containing 200 μM H_2O_2 measured by DLS. (k) CLSM images of the internalization of Th^{Ribo}. Scale bars: 50 μm.

0.80–0.83 between Th^{Ribo} and ribosomes, significantly higher than the 0.22–0.41 observed for the non-targeting control group. Furthermore, the Pearson's correlation coefficient between Th^{Ribo} and lysosomes was 0.27, confirming effective lysosomal escape (Fig. S12 in the ESM). These results collectively validate the specific ribosome-targeting ability of Th^{Ribo} in living cells. These results demonstrate the potential of the nanochaperone in the application of maintaining proteostasis.

2.2 Th^{Ribo}-mediated proteostasis maintenance effect for aging prevention and reversal

Thioredoxin (Trx) is a highly conserved cellular redox regulator, pivotal for maintaining redox homeostasis and mediating thiol–disulfide exchange reactions [35, 36]. By facilitating the reduction of critical protein disulfide bonds, Trx safeguards proteins from oxidative damage and modulates their activity, and thus is frequently employed as a tag for protein expression to perform as a chaperone. Previous studies have proven that Trx safeguards proteins from oxidative damage and modulates their activity [36–38]. Consequently, the efficient intracellular delivery of peptides and their subsequent targeting to ribosomes holds considerable significance for the maintenance of intracellular proteostasis. To evaluate the proteostasis-maintaining effect, we used the common cell line human embryonic kidney 293 (HEK293) to construct the pre-aging cell model and evaluate the global synthesis, thiol oxidation, protein oxidation, and protein carbonylation.

Firstly, we utilized high doses of D-galactose (50 mg/mL) to induce intracellular ROS production as the pre-aging cell model. As shown in Figs. 2(a) and 2(b), the copper-catalyzed click chemistry assay was conducted for analyzing ribosome biogenesis. A clear decrease in global protein synthesis occurred in the pre-aging HEK293 cells. Compared to Th^{-HTrx} without ribosome-targeted probes modification, Th^{Ribo} alleviated the reduction in protein synthesis induced by oxidative stress. Next, the intracellular oxidation of protein was measured by the advanced oxidation protein products (AOPPs) assay. The CLSM imaging and statistical analysis of the enzyme-linked immunosorbent assay (ELISA) suggested Th^{Ribo} significantly reduced the oxidized protein in pre-aging cells (Figs. 2(c) and 2(d)).

Biotinylated BTD is a benzothiazine-derived probe that covalently binds to the sulfenic acid form of oxidized cysteine [15, 39]. In the BTD assay, the cell oxidative stress induced by adding D-galactose caused an increase in thiol oxidation (Fig. 2(e)). The treatment of Th^{-HTrx} exerted a change on the oxidation of thiols, which may be caused by the reductive HTrx, while the treatment of Th^{Ribo} significantly decreased the thiol oxidation level in 24 h, indicating the ribosome-targeted strategy is critical for directly interfering with the newly synthesized protein (Fig. S13 in the ESM). Cysteine is frequently highly conserved within functional protein domains (regulatory, catalytic, and binding). This conservation is attributed to the unique thiol/thiolate chemistry of cysteine, which confers specialized properties like nucleophilicity, high-affinity metal coordination, and the ability to form disulfide bonds onto these sites [40, 41]. Hence, the protection of thiol from oxidation is crucial for maintaining intracellular proteostasis. In the protein carbonylation assay as shown in (Figs. 2(f) and 2(g)), consistent with the results of anti-thiol oxidation, ThRibo exhibited a superior carbonylation depression effect in pre-aging cells. In conclusion, it can be determined that Th^{Ribo} with ribosome-targeted modification can effectively defend the newly synthesized protein against oxidative damage in pre-aging cells. Moreover, Th^{Ribo}

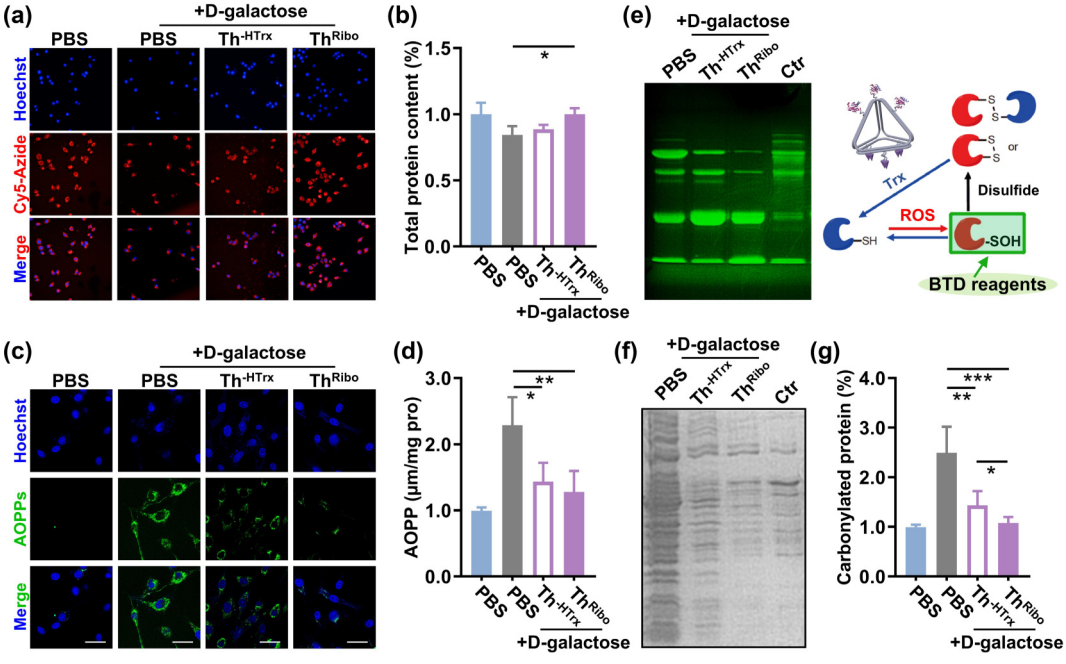

Figure 2 Proteostasis maintenance and prevention of cellular aging by Th^{Ribo}. (a) and (b) Copper-catalyzed click chemistry assay using Cy5-Azide. Global protein synthesis was measured by high-content screening as red fluorescence signal per cell (PE, Opera Phenix High Content Screening System). (c) and (d) AOPPs level in pre-aging HEK293 cells. (e) BTD assay of extracted protein in pre-aging HEK293 under different treatments (100 nM of Th^{-HTrx} or Th^{Ribo}). Normal HEK293 cells were utilized as control. Biotinylated BTD (1 mM) was mixed in the lysis solution as an indicator. (f) and (g) Protein carbonylation analysis of HEK293 under different treatments. The total protein extracted from HEK293 cells was pre-reacted with 2,4-dinitrophenylhydrazine (DNPH) and separated by SDS-PAGE. To build the pre-aging cell model, HEK293 cells were treated with 50 mg/mL D-galactose for 24 h, then 100 nM of Th^{-HTrx} or Th^{Ribo} was administered and cultured for a further 24 h. Data are presented as mean ± standard deviation (SD) ($n = 3$). *$P < 0.05$; **$P < 0.01$; ***$P < 0.001$.

exhibited the ability to shield intracellular nucleic acids against oxidative damage, and furthermore, it can facilitate cellular proliferation in normal or oxidative stress microenvironment (Figs. S14 and S15 in the ESM).

Next, the proteostasis-maintaining effect of Th^{Ribo} was tested on the aging cell model induced by directly adding H_2O_2. In contrast with the pre-aging cell induced by culturing with D-galactose, which induces cellular senescence primarily through the accumulation of advanced glycation end-products as chronic oxidative stress [42–44], the cells stimulated by H_2O_2 sharply turn to a state of oxidative stress with an imbalance of oxidation–reduction in the cytoplasm. In the copper-catalyzed click chemistry assay, a decrease in global protein synthesis was still measured within aging HEK293 cells as shown in Figs. 3(a) and 3(b). Compared to the untargeted Th^{-HTrx}, the ribosome-targeted Th^{Ribo} significantly alleviated this oxidative stress-induced reduction. Subsequently, the AOPPs assay, combined with CLSM and ELISA-based statistical analysis, demonstrated that Th^{Ribo} significantly reduced oxidized protein levels in aging cells as expected (Figs. 3(c) and 3(d)). In the BTD assay, H_2O_2-induced oxidative stress elevated intense thiol oxidation (Fig. 3(e)). Th^{Ribo} treatment significantly decreased thiol oxidation within 24 h, while Th^{-HTrx} treatment had a slight effect, which is likely due to the inherent reductase activity of HTrx as mentioned. This result once again underscores the critical role of ribosome targeting in directly protecting nascent proteins. Th^{Ribo} also exhibited a superior ability to suppress protein carbonylation in aging cells (Figs. 3(f) and 3(g)). In conclusion, these findings demonstrate that the ribosome-targeted Th^{Ribo} effectively defends newly synthesized proteins and reverses oxidative damage in aging cells. To evaluate the global transcriptional alterations induced by Th^{Ribo} in aging cells, we performed differential gene expression analysis between the PBS and Th^{Ribo} treatment groups. As shown in Fig. 3(h), Th^{Ribo} treatment resulted in significant transcriptional reprogramming, characterized by the identification of distinct upregulated and downregulated genes across multiple functional categories. Furthermore, Kyoto Encyclopedia of Genes and

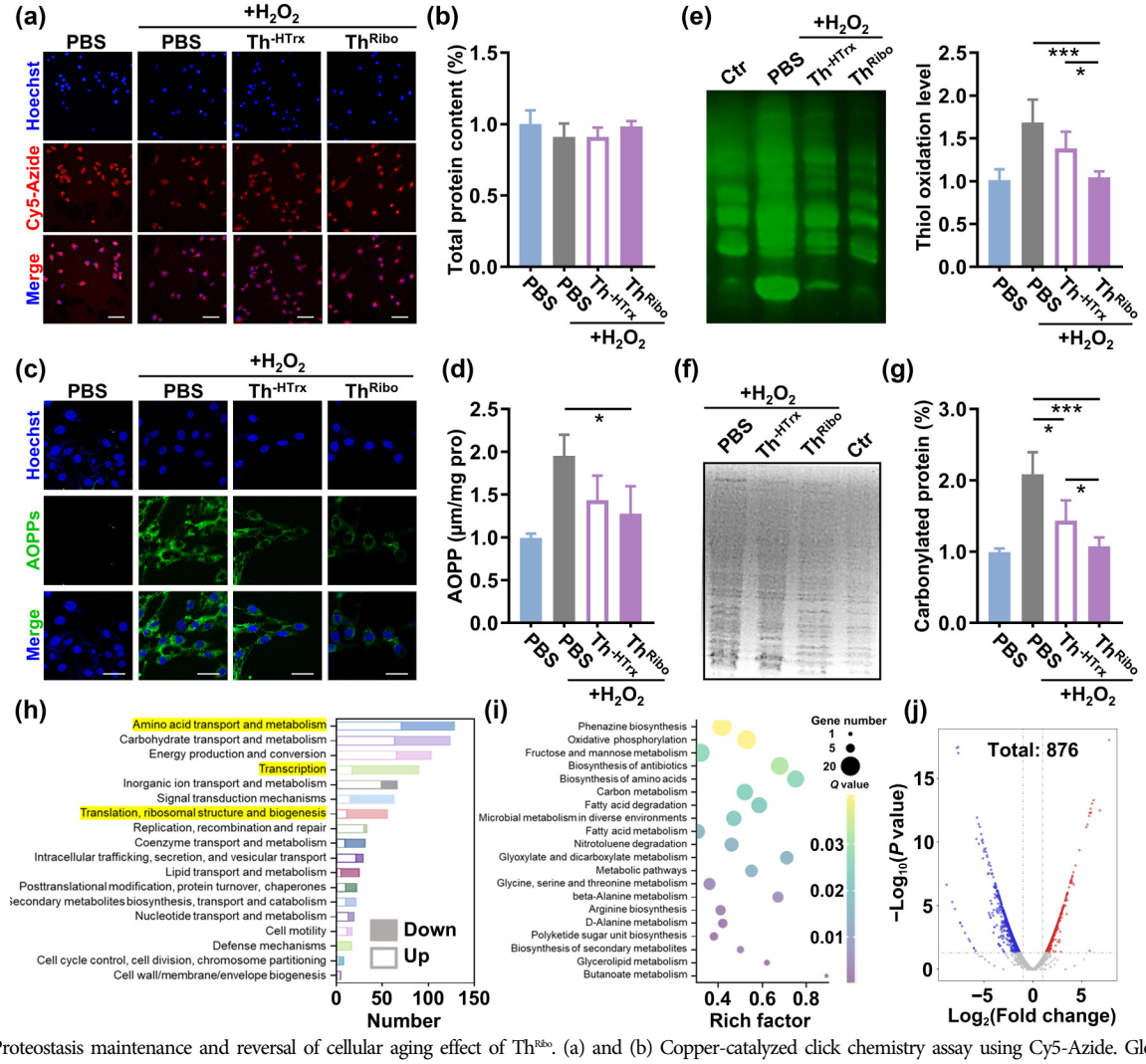

Figure 3 Proteostasis maintenance and reversal of cellular aging effect of Th^{Ribo}. (a) and (b) Copper-catalyzed click chemistry assay using Cy5-Azide. Global protein synthesis was measured by high-content screening as red fluorescence signal per cell. (c) and (d) AOPPs level in aging HEK293 cells. (e) BTD assay of extracted protein in aging HEK293 under different treatments (100 nM of Th^{-HTrx} or Th^{Ribo}). Normal HEK293 cells were utilized as control. Biotinylated BTD (1 mM) was mixed in the lysis solution as indicator. (f) and (g) Protein carbonylation analysis of HEK293 under different treatments. (h) DEGs between the PBS and Th^{Ribo} treatments on aging cells. (i) KEGG pathway enrichment analysis. (j) Volcano plots of the identified upregulated and down-regulated genes between the PBS and Th^{Ribo} treatment. To build the aging cell model, HEK293 cells were treated with 200 μM H_2O_2 for 6 h, then 100 nM of Th^{-HTrx} or Th^{Ribo} were administered and cultured for a further 24 h. Data are presented as mean ± SD ($n = 3$). *$P < 0.05$; **$P < 0.01$; ***$P < 0.001$.

Genomes (KEGG) pathway enrichment analysis of the differentially expressed genes (DEGs) revealed that Th^{Ribo} predominantly modulates several critical biological processes related to metabolic regulation, including oxidative phosphorylation, amino acid biosynthesis, and carbon metabolism (Fig. 3(i)). The volcano plot further illustrates the overall distribution of upregulated and downregulated genes between the PBS and Th^{Ribo} treatment groups (Fig. 3(j)). Thus, the Th^{Ribo} significantly impacts biological processes associated with transcription, ribosome structure and biogenesis, as well as amino acid transport and metabolism.

2.3 Oxidative protection and aging resistance effect of Th^{Ribo} in neural cells

After confirming the effect of Th^{Ribo} in maintaining proteostasis, we then tested the protective efficacy against oxidative damage in various cell lines. As the functional element adopted in constructing the nanochaperone demonstrates universal applicability irrespective of species, we subsequently carried out a series of tests in human-derived U-87 MG (U87) cell and murine-derived BV-2 (BV2) cell (Figs. S16 and S17 in the ESM). We first verified the protein carbonylation analysis in normal (as control) and aging cells. After the treatment of Th^{Ribo}, the carbonylated protein level was close to that of normal cells (U87: 117.1% ± 6.0%; BV2: 109.6% ± 9.5%) without H_2O_2 stimulation (Figs. 4(a) and 4(b)). The results of the AOPPs assay also revealed that Th^{Ribo} holds a significant effect in reducing oxidized protein products in both U87 cells and BV2 cells (Figs. S18 and S19 in the ESM). As illustrated in Fig. 4(c), intracellular proteins are highly susceptible to oxidative modification under the aging microenvironment, particularly at residues like cysteine, methionine, and histidine, disrupting their structure and function. This often manifests as reduced enzymatic activity. Furthermore, the oxidative cascade extends to membrane lipids, promoting peroxidation that compromises integrity and generates propagating reactive byproducts. Mitochondria, as key ROS sources and targets, frequently suffer dysfunction under oxidative stress, marked by membrane potential dissipation [45–47]. Hence, we first measured the intracellular ROS level by CLSM imaging. The administration of Th^{Ribo} significantly reduced the ROS level in both kinds of cells in 24 h (Figs. 4(d) and 4(i), and Figs. S20–S25 in the ESM), while the control experiments confirm that the DNA nanocarrier itself exerts negligible non-specific effects, thereby validating that the therapeutic efficacy is specifically attributed to the loaded HTrx. The oxidative damage of nucleic acids was also inhibited under the treatment (Figs. S26 and S27 in the ESM). Correspondingly, the glutathione disulfide (GSSG) level

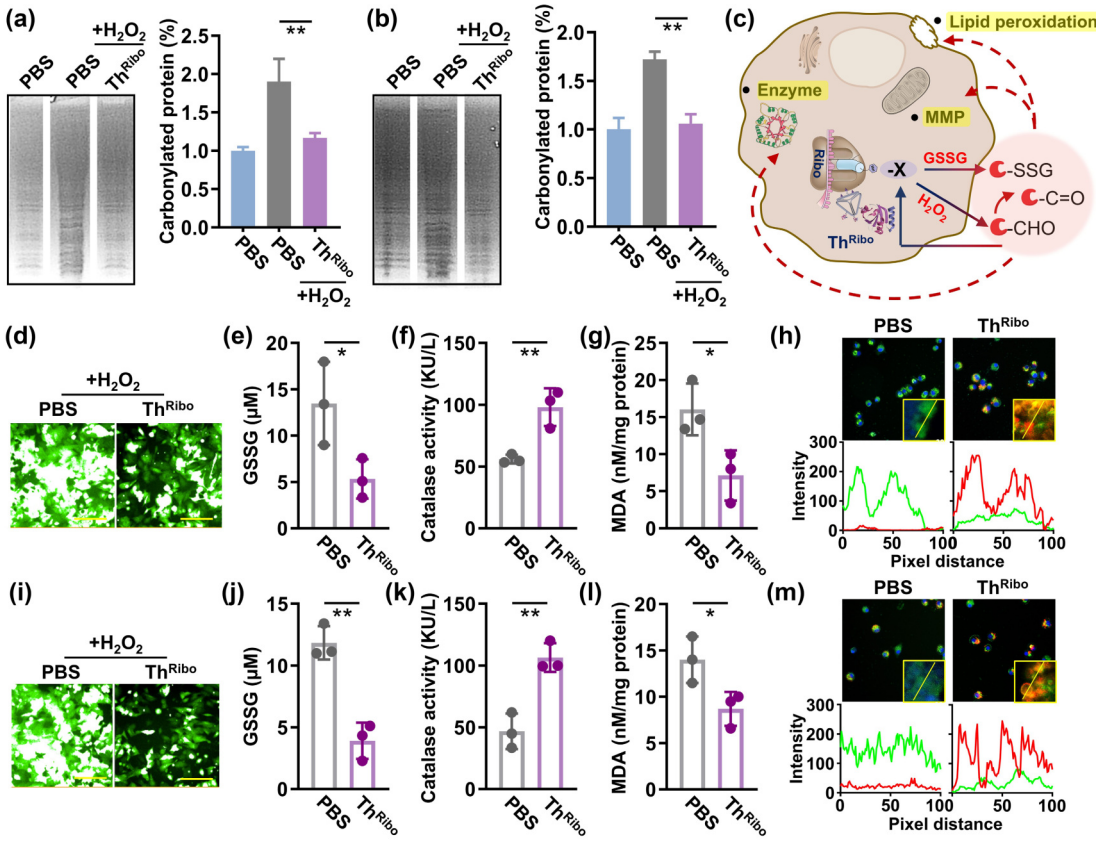

Figure 4 Protective effect of Th^{Ribo} against oxidative damage in aging neural cells. (a) Protein carbonylation analysis of aging U87 cells under the treatment of Th^{Ribo}. (b) Protein carbonylation analysis of aging BV2 cells under different treatments. (c) Illustration of the proteostasis maintaining effect on enzyme activity, MMP, and lipid peroxidation. The intracellular ROS level of (d) H_2O_2-induced aging U87 cells and (i) aging BV2 cells incubated with PBS or Th^{Ribo}. Cells were stained with the ROS probe 2',7'-dichlorofluorescein diacetate (DCFH-DA) after the treatment with PBS or Th^{Ribo}. Scale bars: 50 μm. Intracellular GSSG level in (e) aging U87 cells and (j) aging BV2 cells under different treatments. Catalase activity analysis of (f) aging U87 cells and (k) aging BV2 cells under different treatments. MDA level of (g) aging U87 cells and (l) aging BV2 cells under different treatments measured by ELISA assay. JC-1 imaging of (h) aging U87 cells and (m) aging BV2 cells. Red fluorescence represents a high MMP, while green fluorescence represents a low MMP. The line scan profile of the fluorescence intensity was measured by ImageJ. To build the aging cell model, cells were pretreated with 200 μM H_2O_2 for 6 h, then 100 nM of Th^{Ribo} was administered and cultured for a further 24 h. Data are presented as mean ± SD (n = 3). *P < 0.05; **P < 0.01.

sharply decreased under the treatment of the nanochaperone compared to PBS control (Figs. 4(e) and 4(j)). The excellent oxidative stress inhibition effect was mainly contributed by the synergistic effect of HTrx and the reductive DNA-based nanocarrier [48, 49]. The catalase activity was increased by approximately 1.74 times (U87 cell) and 2.30 times (BV2 cell) under the treatment of ThRibo as shown in (Figs. 4(f) and 4(k)). Meanwhile, the lipid peroxidation marker malondialdehyde (MDA) significantly decreased as expected ((Figs. 4(g) and 4(l))). The change in mitochondrial membrane potential (MMP) was measured by JC-1 staining, demonstrating that the loss of MMP and expression of related signaling pathway caused by oxidative damage were effectively inhibited by Th^{Ribo} administration (Figs. 4(h) and 4(m), and Figs. S28 and S29 in the ESM). Taken together, the nanochaperone Th^{Ribo} effectively mitigates oxidative damage and reverses cellular senescence *in vitro*, suggesting its potential as a therapeutic agent for age-related diseases.

2.4 *In vivo* anti-aging effect of Th^{Ribo} in improving motor function of aged mice

Given aging is accompanied by a decline in cellular proteostasis and reduced ribosomal performance, we performed anti-aging analysis of the nanochaperone in a natural aging mouse model (26 months [50]) as illustrated in Fig. 5(a). Through the analysis of brain tissues obtained post-treatment, Th^{Ribo} treatment significantly reduced the carbonylated protein level (Fig. 5(b)). To evaluate the neurological defects of the aging mouse during the treatment, a set of experiments that reflect the performance of movement, balance, sensory function, and reflexes was utilized in this study. In the Rota-rod test, mice treated with Th^{Ribo} exhibited a significantly longer latency to fall compared to the PBS control group at week 2 and week 3 (Fig. 5(c)), indicating enhanced motor coordination following treatment administration. Furthermore, the dexterity of the contralateral forelimb and hindlimb in aging mice was assessed using the cylinder test and grid test. Aging mice receiving Th^{Ribo} treatment displayed decreased asymmetry scores at weeks 2–3 (Fig. 5(d)) and a reduced asymmetry index at both weeks 2 and 3 (Fig. 5(e)), suggesting improved limb dexterity. Collectively, the nanochaperone treatment significantly promotes functional recovery in aging mice. Compared to the PBS group, the ROS level remarkably decreased according to the results of immunofluorescence (Fig. 5(f)). We also examined the molecular levels of glutathione (GSH), GSSG, MDA, and catalase activity in tissue lysate samples of the two groups. The Th^{Ribo} group exhibited a remarkable decrease in oxidative damage markers GSSG and MDA, and higher catalase activity (Figs. 5(g)–5(j)).

We then proceeded to investigate the *in vivo* mechanisms responsible for conferring resistance to aging. Immunofluorescence analysis exhibited that the treatment of Th^{Ribo} remarkably decreased the level of the aging markers p53, p21, and p16 (Figs. 6(a)–6(c)). As shown in the results of the western blot assay of the brain tissue, the protein levels of p53, p21, and p16 were significantly

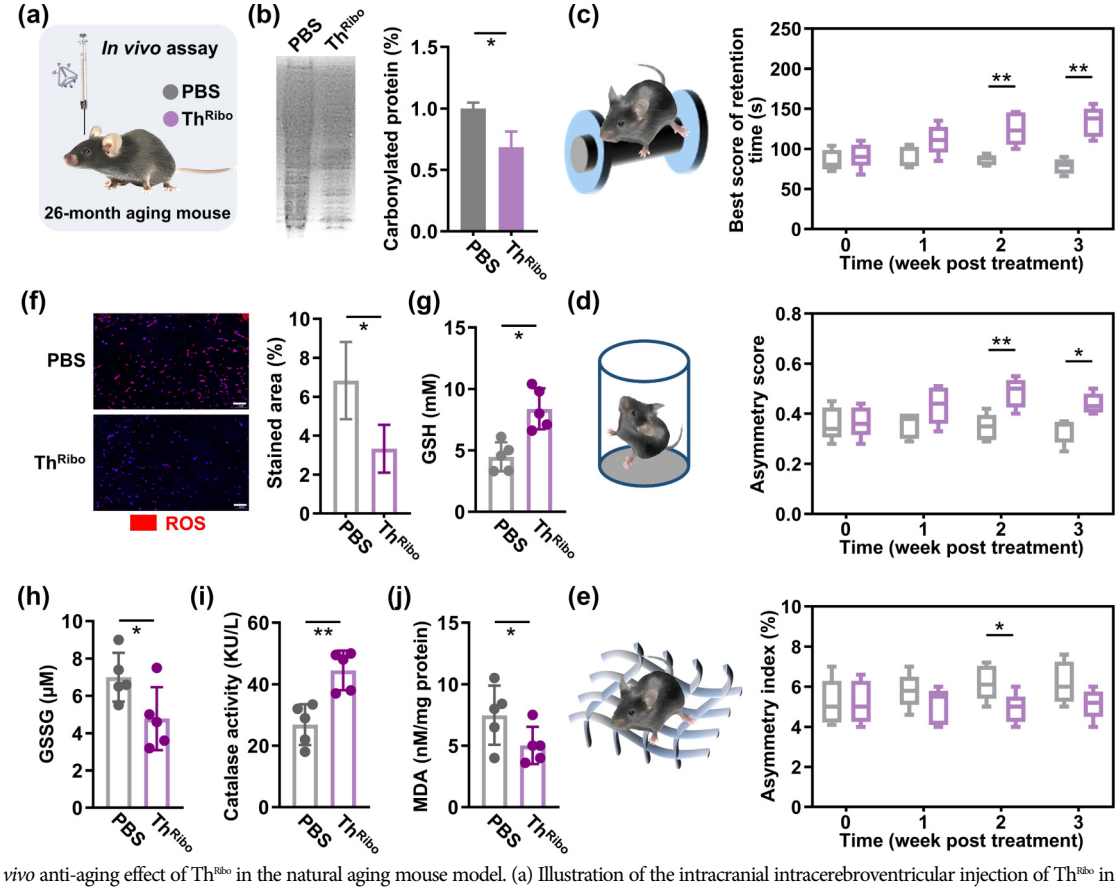

Figure 5 *In vivo* anti-aging effect of Th^{Ribo} in the natural aging mouse model. (a) Illustration of the intracranial intracerebroventricular injection of Th^{Ribo} in a natural aging mouse model. The drug concentration was 2 μM of Th^{Ribo} (5 μL per mouse on week 0 and 1). (b) Protein carbonylation analysis of the brain after different treatments. (c) Rota-rod test, (d) cylinder test, and (e) grid test for motor ability and the dexterity of forelimbs and hindlimbs of mice in different groups over three weeks. (f) ROS imaging of the brain after different treatments. Red fluorescence signal indicates ROS signal. Scale bars: 50 μm. (g) GSH level, (h) GSSG level, (i) catalase activity analysis, and (j) MDA level in brain tissues under different treatments. Data are presented as mean ± SD ($n = 5$). *$P < 0.05$; **$P < 0.01$.

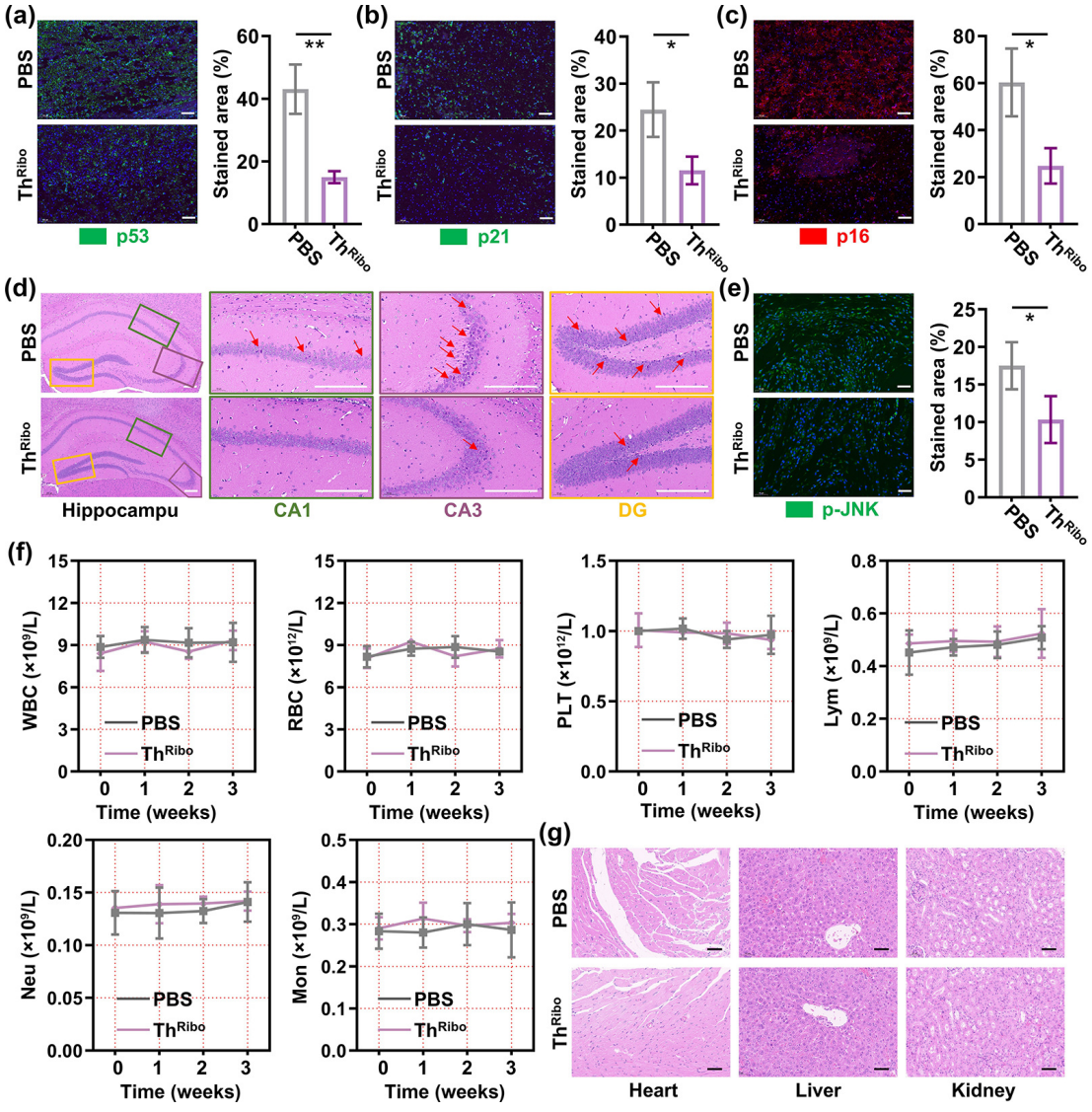

Figure 6 Mechanism analysis of the anti-aging effect of Th^{Ribo} in the natural aging mouse model. Immunofluorescence and statistical analysis of (a) p53 (green fluorescence), (b) p21 (green fluorescence), and (c) p16 (red fluorescence) of the brain after the treatment. Scale bars: 50 μm. (d) H&E staining of the hippocampus and refined structure. Apoptosis-like cells are indicated with a red arrow. Scale bars: 200 μm. (e) p-JNK (green fluorescence) of the brain after the treatment. (f) Routine blood examination of white blood cells (WBC), red blood cells (RBC), platelets (PLT), lymphocytes (Lym), neutrophils (Neu), and monocytes (Mon) during the treatment of Th^{Ribo} on weeks 0, 1, 2, and 3. (g) H&E staining of major organs (heart, liver, and kidney). Scale bars: 50 μm. Data are presented as mean ± SD (n = 5). *P < 0.05; **P < 0.01)

downregulated in the treatment group compared to the control, confirming the inhibition of the senescence-associated signaling axis (Fig. S30 in the ESM). Furthermore, the phosphorylation level of JNK (p-JNK) exhibited a marked decrease, indicating potent inhibition of the stress-responsive JNK pathway (Fig. S31 in the ESM). These biochemical results are consistent with the semi-quantitative fluorescence analysis and quantitative reverse transcription polymerase chain reaction (RT-qPCR) (Figs. S32–S35 in the ESM), providing robust evidence for the proposed mechanism involving the p53/p21/p16 axis-mediated senescence and JNK pathway activation. H&E staining was used to evaluate changes in the histopathological architecture of the hippocampal tissues. As shown in Fig. 6(d), pyramidal neurons in the CA1, CA3, and DG regions were tightly arranged and exhibited round and clear nuclei in the Th^{Ribo} treatment group, whereas, by contrast, the pyramidal neurons were densely stained, exhibited atrophic cytoplasm, apoptosis-like cells were observed as indicated, and had an irregular triangular shape in the PBS group, suggesting a widespread neuronal anti-aging effect. The above results indicate that the artificial chaperone can reverse the oxidative damage in the brain tissue of the aging mice, thereby improving their behavioral performance. Additionally, we noted that the p-JNK level remarkably reduced after the treatment of Th^{Ribo} (Fig. 6(e)), confirming that the nanochaperone exhibits excellent antioxidant efficacy in natural aging mouse models. During the treatment, the routine blood parameters remained within normal ranges, indicating favorable hematological compatibility (Fig. 6(f)). Furthermore, H&E staining of major organs collected after the treatment revealed no noticeable pathological abnormalities or inflammatory lesions, suggesting that Th^{Ribo} does not induce systemic organ toxicity (Fig. 6(g)). Collectively with the results of the body weight monitoring, these results confirm the excellent

biocompatibility and safety profile of Th^{Ribo} for potential biomedical applications (Figs. S36–S38 in the ESM), suggesting that Th^{Ribo} holds significant potential for mitigating damage stemming from proteostasis in the context of aging *in vivo*.

Looking ahead, establishing the clinical potential of Th^{Ribo} necessitates a focused research roadmap addressing key translational challenges. First, regarding targeting precision, future investigations will be directed toward optimizing the structural design to further enhance binding specificity, thereby eliminating potential off-target interactions with non-target RNAs and ensuring precise intervention. Second, to ensure biosafety for clinical application, subsequent studies will explore how to mitigate potential innate immune responses, ensuring the platform remains immunologically inert *in vivo*. These proactive strategies will be pivotal in advancing Th^{Ribo} from a proof-of-concept to a viable therapeutic modality for aging-related proteostasis disorders.

3 Experimental

3.1 Expression and purification of the recombinant HTrx and HTrx-S

The plasmid pET-28a-His-Trx-C was constructed for expression of HTrx with an N-terminal His_6-tag and a C-terminal-$(GS)_3$-C sequence as previously described [51]. The cysteine residues (–C) were introduced for conjugation with the single-strand DNA (ssDNA). The plasmid was transformed into *E. coli* Rosetta-gami cells and protein expression was induced by isopropyl-*β*-D-thiogalactopyranoside (IPTG) (0.4 mM). After being induced overnight (around 12 h), the cells were harvested by centrifugation at 5000 rpm for 15 min.

The precipitates collected by centrifugation were resuspended in binding buffer (20 mM Tris-HCl, 150 mM NaCl, pH = 8.0). After ultrasonic treatment, cell lysates were centrifuged at 16,000 rpm for 25 min at 4 °C. The recombinant protein was purified using a nickel-nitrilotriacetic acid (Ni-NTA) column (His-Trap HP column 5 mL, GE Healthcare) with a linear gradient of 10–250 mM imidazole in binding buffer. The protein concentration was measured with the Bradford assay and the purity was analyzed by sodium dodecyl sulfate-polyacrylamide gel electrophoresis (SDS-PAGE).

HTrx was coupled to ssDNA strand (5'-NH_2-TTC AGA GGC GCT-3') using sulfo-SMCC conjugation. The amino-modified ssDNA was diluted with PBS (pH = 7.4) at a concentration of 100 μM. The solution of amino-modified oligonucleotide was mixed with sulfo-SMCC (25 eq. relative to amino-modified ssDNA) and reacted at 25 °C for 10 h. After that, the additional sulfo-SMCC was removed by 10 kDa molecular weight cut-off (MWCO) centrifuge filters three times to obtain SMCC-ssDNA. At the same time, HTrx was purified in PBS buffer using desalting columns (HiTrap™ Desalting) on an ÄKTA purifier system (GE Healthcare). The reduced HTrx was mixed with purified SMCC-ssDNA in a ratio of 2.5:1 to prepare the HTrx-DNA conjugate, namely HTrx-S. After 6 h of incubation at room temperature, HTrx-S was purified using gel filtration through an ÄKTA purifier system equipped with a HiLoad 10/60 Superdex 200 column. The chromatograph was monitored at 254 and 280 nm. The concentration of HTrx was measured using the bicinchoninic acid (BCA) assay based on HTrx and the purity was analyzed by SDS-PAGE.

3.2 Design and assembly of the DNA nanochaperone

The nanocarrier DNA tetrahedron was assembled according to our method with some modifications [1]. DNA sequences used in this study for assembly are shown in Table S1 in the ESM. Firstly, the accurately quantified DNA strands (100 nM) were equally mixed in a 1× TAE/Mg^{2+} buffer (pH = 8.3), respectively. The aforementioned assembly samples were kept at 95 °C (5 min) and then cooled down to 37 °C within 1 h as reported. Then four groups (V-1, V-2, V-3, and V-4) and HTrx-S were assembled with a molecular ratio of 1:1:1:1:3. Then the mixture was cooled down from 37 to 25 °C in 12 h and the prepared Th^{Ribo} was stored at 4 °C.

3.3 Characterization of Th^{Ribo}

The prepared Th^{Ribo} (100 nM, 10 μL) was deposited onto freshly cleaved mica and allowed to deposit for 10 min. The prepared samples were imaged with a MultiMode 8 AFM (Bruker) under ScanAsyst-Fluid mode. DLS analysis of the DNA tetrahedron and Th^{Ribo} (100 nM cultured in DMEM) was performed on a Malvern Zetasizer Nano-ZS (Malvern Instruments, UK).

4 Conclusions

In this study, a programmable DNA framework-based artificial chaperone, Th^{Ribo}, was constructed by integrating a ribosome-targeted probe and the redox regulator HTrx onto an addressable DNA tetrahedron. DNA nanotechnology enables the construction of nanostructures with precise spatial control via programmable Watson–Crick base pairing. In this work, we utilized a double-bundle DNA tetrahedron, developed by our team, which integrates high structural stability, synthesis yield, and precise addressability. This rigid architecture ensures optimal spatial orientation of HTrx and ribosome-targeting motifs, minimizing steric hindrance and facilitating efficient ribosome engagement. These features distinguish our design from flexible DNA assemblies, allowing for the construction of a robust, plug-and-play artificial chaperone that modulates proteostasis directly at the source of protein synthesis. Th^{Ribo} selectively targets ribosomes and employs a reductive repair cascade to protect newly synthesized peptides from oxidative modifications, including carbonylation and thiol oxidation, thereby stabilizing amino acid residues and restoring proteostasis in aging cells. This protection mitigates enzymatic inactivation, inhibits lipid peroxidation, and prevents the loss of MMP, preserving cellular function both *in vitro* and *in vivo*. In aging mice, Th^{Ribo} effectively suppressed senescence-associated signaling pathways, including the canonical p53/p21/p16 axis and the stress-responsive JNK pathway, improved brain protein homeostasis, reduced oxidative stress markers, enhanced motor performance, and exhibited desirable biocompatibility. Considering the established correlation between proteostasis imbalance and aging, and the critical role of proteostasis in the transition from cellular vitality to senescence, this ribosome-targeted nanochaperone provides a versatile platform for maintaining protein homeostasis and expands the potential of ribosome-targeted therapeutic strategies for anti-aging interventions.

Electronic Supplementary Material: Supplementary material (further details of the experimental protocols, including materials, characterization, cell culture, animal model, RNA-sequencing, immunofluorescence, and statistical analysis) is available in the online version of this article at https://doi.org/10.26599/NR.2026.94908731.

Data availability

All data needed to support the conclusions in the paper are presented in the manuscript and the Electronic Supplementary Material. Additional data related to this paper may be requested from the corresponding author upon request.

Acknowledgements

This work was supported by the National Natural Science Foundation of China (Nos. 82460400 and 82202532), Hainan Provincial Natural Science Foundation of China (No. 824QN261), Hainan Provincial Foreign Expert Project (No. H20260407042E), Academic Enhancement Support Program of Hainan Medical University (No. XSTS2025107), Education Department of Hainan Province (No. Hnky2023-23), start-up fund from Shandong Cancer Hospital (No. rcyj-202603). The authors are grateful for the support of instruments and facilities provided by the Public Research Center of Hainan Medical University.

Declaration of competing interest

All the contributing authors report no conflict of interests in this work.

Author contribution statement

T. T. W.: Data curation, project administration, validation, writing manuscript, experimental design. S. Z., L. L., C. L., and P. X. Z: Data curation and validation. X. Y. C., and J. J. C.: Project administration, funding acquisition, writing manuscript. All the authors have approved the final manuscript.

Informed consent

Not applicable.

Ethics statement

The animal experiments were carried out following the guidelines of the Ethical Committee of Hainan Medical University, which approved the protocol (Ethics code: HYLL-2024-253).

Use of AI statement

During the preparation of this work, the authors used ChatGPT 5.0 in order to polish the language. After using this tool, the authors reviewed and edited the content as needed and take full responsibility for the content of the publication.

References

[1] Stein, K. C.; Morales-Polanco, F.; Van Der Lienden, J.; Rainbolt, T. K.; Frydman, J. Ageing exacerbates ribosome pausing to disrupt cotranslational proteostasis. *Nature* **2022**, *601*, 637–642.

[2] Kaushik, S.; Cuervo, A. M. Proteostasis and aging. *Nat. Med.* **2015**, *21*, 1406–1415.

[3] Hipp, M. S.; Kasturi, P.; Hartl, F. U. The proteostasis network and its decline in ageing. *Nat. Rev. Mol. Cell Biol.* **2019**, *20*, 421–435.

[4] Niforou, K.; Cheimonidou, C.; Trougakos, I. P. Molecular chaperones and proteostasis regulation during redox imbalance. *Redox Biol.* **2014**, *2*, 323–332.

[5] Kehm, R.; Baldensperger, T.; Raupbach, J.; Höhn, A. Protein oxidation-formation mechanisms, detection and relevance as biomarkers in human diseases. *Redox Biol.* **2021**, *42*, 101901.

[6] Glorieux, C.; Liu, S. H.; Trachootham, D.; Huang, P. Targeting ROS in cancer: Rationale and strategies. *Nat. Rev. Drug Discov.* **2024**, *23*, 583–606.

[7] Balch, W. E.; Morimoto, R. I.; Dillin, A.; Kelly, J. W. Adapting proteostasis for disease intervention. *Science* **2008**, *319*, 916–919.

[8] Santra, M.; Dill, K. A.; De Graff, A. M. R. Proteostasis collapse is a driver of cell aging and death. *Proc. Natl. Acad. Sci. USA* **2019**, *116*, 22173–22178.

[9] Gladyshev, V. N.; Kritchevsky, S. B.; Clarke, S. G.; Cuervo, A. M.; Fiehn, O.; De Magalhães, J. P.; Mau, T.; Maes, M.; Moritz, R. L.; Niedernhofer, L. J. et al. Molecular damage in aging. *Nat. Aging* **2021**, *1*, 1096–1106.

[10] Sies, H.; Belousov, V. V.; Chandel, N. S.; Davies, M. J.; Jones, D. P.; Mann, G. E.; Murphy, M. P.; Yamamoto, M.; Winterbourn, C. Defining roles of specific reactive oxygen species (ROS) in cell biology and physiology. *Nat. Rev. Mol. Cell Biol.* **2022**, *23*, 499–515.

[11] Zhu, H. M.; Chen, J. W.; Liu, K. P.; Gao, L.; Wu, H. Y.; Ma, L. L.; Zhou, J. R.; Liu, Z. M.; Han, J. D. J. Human PBMC scRNA-seq-based aging clocks reveal ribosome to inflammation balance as a single-cell aging hallmark and super longevity. *Sci. Adv.* **2023**, *9*, eabq7599.

[12] Joazeiro, C. A. P. Mechanisms and functions of ribosome-associated protein quality control. *Nat. Rev. Mol. Cell Biol.* **2019**, *20*, 368–383.

[13] Llewellyn, J.; Hubbard, S. J.; Swift, J. Translation is an emerging constraint on protein homeostasis in ageing. *Trends Cell Biol.* **2024**, *34*, 646–656.

[14] Ramakrishnan, V. Ribosome structure and the mechanism of translation. *Cell* **2002**, *108*, 557–572.

[15] Yang, Y. M.; Jung, Y.; Abegg, D.; Adibekian, A.; Carroll, K. S.; Karbstein, K. Chaperone-directed ribosome repair after oxidative damage. *Mol. Cell* **2023**, *83*, 1527–1537.e5.

[16] Hartl, F. U.; Bracher, A.; Hayer-Hartl, M. Molecular chaperones in protein folding and proteostasis. *Nature* **2011**, *475*, 324–332.

[17] Doyle, S. M.; Genest, O.; Wickner, S. Protein rescue from aggregates by powerful molecular chaperone machines. *Nat. Rev. Mol. Cell Biol.* **2013**, *14*, 617–629.

[18] Bukau, B.; Weissman, J.; Horwich, A. Molecular chaperones and protein quality control. *Cell* **2006**, *125*, 443–451.

[19] Kim, Y. E.; Hipp, M. S.; Bracher, A.; Hayer-Hartl, M.; Ulrich Hartl, F. Molecular chaperone functions in protein folding and proteostasis. *Annu. Rev. Biochem.* **2013**, *82*, 323–355.

[20] Seeman, N. C.; Sleiman, H. F. DNA nanotechnology. *Nat. Rev. Mater.* **2018**, *3*, 17068.

[21] Li, S. P.; Jiang, Q.; Liu, S. L.; Zhang, Y. L.; Tian, Y. H.; Song, C.; Wang, J.; Zou, Y. G.; Anderson, G. J.; Han, J. Y. et al. A DNA nanorobot functions as a cancer therapeutic in response to a molecular trigger *in vivo*. *Nat. Biotechnol.* **2018**, *36*, 258–264.

[22] Sigl, C.; Willner, E. M.; Engelen, W.; Kretzmann, J. A.; Sachenbacher, K.; Liedl, A.; Kolbe, F.; Wilsch, F.; Aghvami, S. A.; Protzer, U. et al. Programmable icosahedral shell system for virus trapping. *Nat. Mater.* **2021**, *20*, 1281–1289.

[23] Veneziano, R.; Moyer, T. J.; Stone, M. B.; Wamhoff, E. C.; Read, B. J.; Mukherjee, S.; Shepherd, T. R.; Das, J.; Schief, W. R.; Irvine, D. J. et al. Role of nanoscale antigen organization on B-cell activation probed using DNA origami. *Nat. Nanotechnol.* **2020**, *15*, 716–723.

[24] Yin, F. F.; Zhao, H. P.; Lu, S. S.; Shen, J. W.; Li, M.; Mao, X. H.; Li, F.; Shi, J. Y.; Li, J.; Dong, B. J. et al. DNA-framework-based multidimensional molecular classifiers for cancer diagnosis. *Nat. Nanotechnol.* **2023**, *18*, 677–686.

[25] Dong, Y. H.; Yao, C.; Zhu, Y.; Yang, L.; Luo, D.; Yang, D. Y. DNA functional materials assembled from branched DNA: Design, synthesis, and applications. *Chem. Rev.* **2020**, *120*, 9420–9481.

[26] Hu, Q. Q.; Li, H.; Wang, L. H.; Gu, H. Z.; Fan, C. H. DNA nanotechnology-enabled drug delivery systems. *Chem. Rev.* **2019**, *119*, 6459–6506.

[27] Kwon, P. S.; Ren, S. K.; Kwon, S. J.; Kizer, M. E.; Kuo, L. L.; Xie, M.; Zhu, D.; Zhou, F.; Zhang, F. M.; Kim, D. et al. Designer DNA architecture offers precise and multivalent spatial pattern-recognition for viral sensing and inhibition. *Nat. Chem.* **2020**, *12*, 26–35.
[28] Morshedi Rad, D.; Alsadat Rad, M.; Razavi Bazaz, S.; Kashaninejad, N.; Jin, D. Y.; Ebrahimi Warkiani, M. A comprehensive review on intracellular delivery. *Adv. Mater.* **2021**, *33*, 2005363.
[29] Khatter, H.; Myasnikov, A. G.; Natchiar, S. K.; Klaholz, B. P. Structure of the human 80S ribosome. *Nature* **2015**, *520*, 640–645.
[30] Cheng, Y. X.; Qu, Z.; Jiang, Q.; Xu, T. T.; Zheng, H. Y.; Ye, P.; He, M. D.; Tong, Y. Q.; Ma, Y.; Bao, A. Y. Functional materials for subcellular targeting strategies in cancer therapy: Progress and prospects. *Adv. Mater.* **2025**, *37*, 2305095.
[31] Lv, Z. Y.; Huang, M. X.; Yang, J.; Li, P. R.; Chang, L. L.; Tang, Q. Y.; Chen, X. J.; Wang, S. Q.; Yao, C.; Liu, P. F.; Yang, D. Y. A smart DNA-based nanosystem containing ribosome-regulating siRNA for enhanced mRNA transfection. *Adv. Mater.* **2023**, *35*, 2300823.
[32] Wu, T. T.; Zhao, P. X.; Pan, P. C.; Zhao, Z. Q.; Zhu, Y.; Cheng, J. J. Biofilm-disrupting DNA nanomedicines for targeted elimination of resistant wound microbiota. *J. Control. Release* **2025**, *381*, 113618.
[33] Wang, Y. B.; Fu, X. M.; Zhu, Y.; Lin, M. J.; Cai, R. D.; Zhu, Y.; Wu, T. T. An intratumor bacteria-targeted DNA nanocarrier for multifaceted tumor microenvironment intervention. *Mater. Today Bio* **2024**, *27*, 101144.
[34] Wu, T. T.; Liu, J. B.; Liu, M. M.; Liu, S. L.; Zhao, S.; Tian, R.; Wei, D. S.; Liu, Y. Z.; Zhao, Y.; Xiao, H. H. et al. A nanobody-conjugated DNA nanoplatform for targeted platinum-drug delivery. *Angew. Chem., Int. Ed.* **2019**, *58*, 14224–14228.
[35] Gromer, S.; Urig, S.; Becker, K. The thioredoxin system-from science to clinic. *Med. Res. Rev.* **2004**, *24*, 40–89.
[36] Fritz-Wolf, K.; Kehr, S.; Stumpf, M.; Rahlfs, S.; Becker, K. Crystal structure of the human thioredoxin reductase-thioredoxin complex. *Nat. Commun.* **2011**, *2*, 383.
[37] Holmgren, A. Antioxidant function of thioredoxin and glutaredoxin systems. *Antioxid. Redox Signal.* **2000**, *2*, 811–820.
[38] Du, H.; Kim, S.; Hur, Y. S.; Lee, M. S.; Lee, S. H.; Cheon, C. I. A cytosolic thioredoxin acts as a molecular chaperone for peroxisome matrix proteins as well as antioxidant in peroxisome. *Mol. Cells* **2015**, *38*, 187–194.
[39] Shi, Y. L.; Fu, L.; Yang, J.; Carroll, K. S. Wittig reagents for chemoselective sulfenic acid ligation enables global site stoichiometry analysis and redox-controlled mitochondrial targeting. *Nat. Chem.* **2021**, *13*, 1140–1150.
[40] Poole, L. B. The basics of thiols and cysteines in redox biology and chemistry. *Free Radic. Biol. Med.* **2015**, *80*, 148–157.
[41] Fu, L.; Jung, Y.; Tian, C. P.; Ferreira, R. B.; Cheng, R. F.; He, F. C.; Yang, J.; Carroll, K. S. Nucleophilic covalent ligand discovery for the cysteine redoxome. *Nat. Chem. Biol.* **2023**, *19*, 1309–1319.
[42] Bo-Htay, C.; Palee, S.; Apaijai, N.; Chattipakorn, S. C.; Chattipakorn, N. Effects of d-galactose-induced ageing on the heart and its potential interventions. *J. Cell. Mol. Med.* **2018**, *22*, 1392–1410.
[43] Wang, P. P.; Sun, H. X.; Liu, C. J.; Hu, M. H.; He, X. Q.; Yue, S.; Jiao, Z. Z.; Xiang, L. Racemic oleracein E increases the survival rate and attenuates memory impairment in D-galactose/$NaNO_2$-induced senescent mice. *Phytomedicine* **2016**, *23*, 460–467.
[44] Ghanbari, A.; Danaie Fard, P.; Azarmehr, N.; Mahmoudi, R.; Roozbehi, A.; Zibara, K.; Hosseini, E. D-galactose induces senescence in adult mouse neural stem cells by imbalanced oxidant and antioxidant activity and differential expression of specific hub genes. *Mol. Neurobiol.* **2025**, *62*, 4250–4263.
[45] Yang, S.; Zhang, T. Y.; Ge, Y. L.; Cheng, Y. P.; Yin, L. H.; Pu, Y. P.; Chen, Z. Z.; Liang, G. Y. Ferritinophagy mediated by oxidative stress-driven mitochondrial damage is involved in the polystyrene nanoparticles-induced ferroptosis of lung injury. *ACS Nano* **2023**, *17*, 24988–25004.
[46] Liew, S. S.; Qin, X. F.; Zhou, J.; Li, L.; Huang, W.; Yao, S. Q. Smart design of nanomaterials for mitochondria-targeted nanotherapeutics. *Angew. Chem., Int. Ed.* **2021**, *60*, 2232–2256.
[47] Yi, Y.; Xi, X. A.; Huang, L. G.; Liu, X. Y.; Liao, Y. F.; Liu, J. W.; Long, J.; Zhang, J. J.; Fu, X. Z.; Luo, J. L. Boosting the performance and stability of perovskites by construction of NiFe alloy and PrO_x heterogeneously structured composites for high-performance solid oxide fuel cell anode. *Adv. Funct. Mater.* **2025**, *35*, 2412486.
[48] Ge, J. R.; Jia, B.; Wang, Y. A.; Ma, Y. X.; Sun, X. L.; Dong, J.; Jiang, S. X.; Li, Z. DNA nanostructures treat inflammatory bowel disease through ROS scavenging and gut microbiota modulation. *Adv. Funct. Mater.* **2024**, *34*, 2402781.
[49] Wang, H. Y.; Jiao, Y. F.; Ma, S. J.; Li, Z. T.; Gong, J. T.; Jiang, Q.; Shang, Y. X.; Li, H. L.; Li, J.; Li, N. et al. Nebulized inhalation of peptide-modified DNA origami to alleviate acute lung injury. *Nano Lett.* **2024**, *24*, 6102–6111.
[50] Li, B.; Zhang, Q.; Cheng, J. H.; Feng, Y. F.; Jiang, L. X.; Zhao, X. X.; Lv, Y.; Yang, K.; Shi, J. R.; Wei, W. et al. A nanocapsule system combats aging by inhibiting age-related angiogenesis deficiency and glucolipid metabolism disorders. *ACS Nano* **2024**, *18*, 21061–21076.
[51] Wu, T. T.; Huang, H.; Sheng, Y. P.; Shi, H. D.; Min, Y. Z.; Liu, Y. Z. Transglutaminase mediated PEGylation of nanobodies for targeted nano-drug delivery. *J. Mater. Chem. B* **2018**, *6*, 1011–1017.